

Dense and warm molecular gas in the envelopes and outflows of southern low-mass protostars

T. A. van Kempen^{1,2}, E. F. van Dishoeck^{1,3}, M. R. Hogerheijde¹, and R. Güsten⁴

¹ Leiden Observatory, Leiden University, PO Box 9513, 2300 RA Leiden, The Netherlands

² Center for Astrophysics, 60 Garden Street, MS 78, Cambridge, MA 02138, USA
e-mail: tvankempen@cfa.harvard.edu

³ Max Planck Institut für Extraterrestrische Physik (MPE), Giessenbachstr. 1, 85748 Garching, Germany

⁴ Max Planck Institut für Radioastronomie, Auf dem Hügel 69, 53121 Bonn, Germany

Received 7 October 2008 / Accepted 6 October 2009

ABSTRACT

Context. Observations of dense molecular gas lie at the basis of our understanding of the density and temperature structure of protostellar envelopes and molecular outflows. The Atacama Pathfinder EXperiment (APEX) opens up the study of southern ($\text{Dec} < -35^\circ$) protostars.

Aims. We aim to characterize the properties of the protostellar envelope, molecular outflow and surrounding cloud, through observations of high excitation molecular lines within a sample of 16 southern sources presumed to be embedded YSOs, including the most luminous Class I objects in Corona Australis and Chamaeleon.

Methods. Observations of submillimeter lines of CO, HCO⁺ and their isotopologues, both single spectra and small maps (up to $80'' \times 80''$), were taken with the FLASH and APEX-2a instruments mounted on APEX to trace the gas around the sources. The HARP-B instrument on the JCMT was used to map IRAS 15398-3359 in these lines. HCO⁺ mapping probes the presence of dense centrally condensed gas, a characteristic of protostellar envelopes. The rare isotopologues C¹⁸O and H¹³CO⁺ are also included to determine the optical depth, column density, and source velocity. The combination of multiple CO transitions, such as 3–2, 4–3 and 7–6, allows to constrain outflow properties, in particular the temperature. Archival submillimeter continuum data are used to determine envelope masses.

Results. Eleven of the sixteen sources have associated warm and/or dense ($\geq 10^6 \text{ cm}^{-3}$) quiescent gas characteristic of protostellar envelopes, or an associated outflow. Using the strength and degree of concentration of the HCO⁺ 4–3 and CO 4–3 lines as a diagnostic, five sources classified as Class I based on their spectral energy distributions are found not to be embedded YSOs. The C¹⁸O 3–2 lines show that for none of the sources, foreground cloud layers are present. Strong molecular outflows are found around six sources, with outflow forces an order of magnitude higher than for previously studied Class I sources of similar luminosity.

Conclusions. This study provides a starting point for future ALMA and Herschel surveys by identifying truly embedded southern YSOs and determining their larger scale envelope and outflow characteristics.

Key words. astrochemistry – stars: formation – submillimeter – ISM: jets and outflows – ISM: molecules

1. Introduction

During the early stages of low-mass star formation, young stellar objects (YSOs) are embedded in cold dark envelopes of gas and dust, which absorb the radiation from the central star (Lada 1987; André et al. 1993). This extinction is strong enough that low-mass embedded YSOs, or protostars, only emit weakly at infrared wavelengths (e.g., Jørgensen et al. 2005b; Gutermuth et al. 2008). Only at later evolutionary phases, in which the envelope has been accreted and/or dispersed, does emission in the optical and infrared (IR) dominate the spectral energy distribution (SED) (e.g. Hartmann et al. 2005). Protostars emit the bulk of their radiation at far-IR and sub-millimeter wavelengths, both as continuum radiation, produced by the cold ($T < 30 \text{ K}$) dust, and through molecular line emission from the gas-phase species present throughout the protostellar envelope. Although the bulk of the mass is accreted during the earliest embedded phases, more evolved protostellar envelopes still contain a reservoir of gas and dust that can accrete onto the central star and disk system and thus provide the material for disk and planet formation. At the same time, jets and winds from the young star interact with the envelope and drive molecular outflows which clear the

surroundings. Characterizing and quantifying all of these different physical components in the protostellar stage is still a major observational challenge.

The protostellar envelopes and molecular outflows can be directly observed either through thermal emission of dust at (sub)millimeter wavelengths (e.g. Shirley et al. 2000; Johnstone et al. 2001; Nutter et al. 2005) or the line emission of molecules. Low frequency molecular emission traces the cold gas in the protostellar envelopes (e.g., Hogerheijde et al. 1998; Jørgensen et al. 2002; Maret et al. 2004) or molecular outflows (e.g., Snell et al. 1990; Cabrit & Bertout 1992; Bachiller & Tafalla 1999). Single-dish observations of dust using current generation bolometer arrays are able to map large areas and image the surroundings of protostars (e.g., Motte et al. 1998; Shirley et al. 2000; Stanke et al. 2006; Nutter et al. 2008). Through radiative transfer models (e.g., Shirley et al. 2002; Jørgensen et al. 2002; Young et al. 2003), including information from shorter wavelengths (e.g., Hatchell et al. 2007b), the temperature and density structure of the protostellar envelope can be constrained, but the continuum data cannot determine the velocity structure of the infalling envelope, characterize the outflows

and their interaction with the surroundings, or disentangle envelope and (foreground) cloud material. Analysis of gas observations in the form of spectra of multiple transitions of the same molecule and its isotopologues provide additional strong constraints on the physical characteristics of the protostellar envelope (Mangum & Wootten 1993; Blake et al. 1994; van Dishoeck et al. 1995; Schöier et al. 2002; Maret et al. 2004; Jørgensen et al. 2005b; Evans et al. 2005; van der Tak et al. 2007) and outflowing gas (e.g., Cabrit & Bertout 1992; Bontemps et al. 1996; Hogerheijde et al. 1998; Hatchell et al. 1999; Parise et al. 2006; Hatchell et al. 2007a).

Although many different molecules have been observed in protostellar envelopes, only a limited number of species are well suited to trace the physical characteristics of all of the components of an embedded YSO and its surroundings. For example, the use of CH₃OH and H₂CO is complicated by their changing abundances through the envelope, although some information can be obtained with careful analysis and a sufficient number of observed lines (e.g. Mangum & Wootten 1993; Blake et al. 1994; van Dishoeck et al. 1995; van der Tak et al. 2000; Leurini et al. 2004). The weakness of high-excitation CH₃OH and H₂CO lines in all but a handful of the most luminous Class 0 protostars (e.g. Jørgensen et al. 2005a) coupled with a lack of some collisional rate coefficients make these species less suitable tracers for the bulk of the low-mass embedded YSOs. In practice, the column density of the surrounding cloud (and that of any unrelated foreground clouds) is best probed by low excitation optically thin transitions of molecules with a low dipole moment, such as the isotopologues of CO, e.g., C¹⁸O 2–1 or 3–2 (van Kempen et al. 2009b). For molecular outflows the line wings of various ¹²CO transitions have been efficiently used as tracers of their properties (Cabrit & Bertout 1992; Bontemps et al. 1996; Hogerheijde et al. 1998; Bachiller & Tafalla 1999; Hatchell et al. 1999; Hatchell et al. 2007a). The denser regions of the protostellar envelope need to be probed with emission lines with a high critical density, such as the higher excitation transitions from HCO⁺ with critical densities >10⁶ cm⁻³. The warm gas ($T > 50$ K), which can be present in both the molecular outflow and the inner region of the protostellar envelope, can only be traced by spectrally resolved high- J CO transitions, which have $E_{\text{up}} > 50$ K for $J_{\text{up}} \geq 4$ (Hogerheijde et al. 1998).

Embedded YSOs are generally identified by their 2–24 μm IR slope with positive values characteristic of Class I objects (Lada 1987). Over the last several years, it has been found that some of these Class I objects turn out to be edge-on disks or obscured sources (e.g., Luhman & Rieke 1999; Brandner et al. 2000; Pontoppidan et al. 2005; Lahuis et al. 2006; van Kempen et al. 2009b). The use of a spectral line map over a small ($\sim 2' \times 2'$) region around the protostar is an elegant solution to disentangle the contributions of the different components (Boogert et al. 2002). In particular, the spatial distribution of the HCO⁺ 4–3 line has proven to be an excellent diagnostic of such “false” embedded sources: in the case of Ophiuchus, about 60% of the sources with Class I or flat SED slopes turned out not to be embedded YSOs (van Kempen et al. 2009b).

With the development of the Atacama large millimeter/submillimeter array (ALMA) on Chajnantor, Chile, surveys of sources in southern star-forming clouds will be undertaken at high resolution ($\leq 1''$) at a wide range of frequencies, and are expected to reveal much about the inner structure of protostars and their circumstellar disks. The *Herschel* space observatory will also target a large number of low-mass YSOs across the sky. Both sets of observations rely heavily on complementary

large aperture ground-based single-dish observations for planning and interpretation. Apart from providing the necessary information about the structure on larger scales, single-dish studies of low-mass star formation in the southern sky will also put the results obtained from studies on the northern hemisphere in perspective.

Due to a lack of sub-millimeter telescopes at high dry sites in the southern hemisphere, high frequency data on southern YSOs are still limited. The Swedish ESO submillimeter telescope (SEST) operated up to the 345 GHz window, but for only limited periods of the year. As a result, southern clouds, such as Chamaeleon, Corona Australis, Vela or Lupus, are much less studied than their counterparts in the northern sky, such as Taurus and Perseus, where such observations have been readily available for over a decade (e.g., Hogerheijde et al. 1997; Motte et al. 1998; Hogerheijde et al. 1998; Johnstone et al. 2000; Jørgensen et al. 2002; Nutter et al. 2005; Nutter et al. 2008). The Atacama Pathfinder EXperiment (APEX) (Güsten et al. 2006)¹ has opened up access to the atmospheric windows in the 200–1400 μm wavelength regime over the entire southern sky.

Of the southern star-forming regions not or only poorly visible with northern telescopes two regions have proven especially interesting. The Chamaeleon I cloud ($D = 130$ pc, $\text{Dec} = -77^\circ$), observed with *IRAS* and the *Infrared Space Observatory* (ISO) and included in the *Spitzer* space telescope guaranteed time and “Cores to disks” (c2d) Legacy programs (Persi et al. 2000; Evans et al. 2003; Damjanov et al. 2007; Luhman et al. 2008) contains some embedded sources, especially around the Cederblad region (Persi et al. 2000; Lehtinen et al. 2001; Belloche et al. 2006; Hiramatsu et al. 2007). Corona Australis is a nearby star-forming region ($D = 170$ pc, see Knude & Høg (1998); $\text{Dec} = -36^\circ$), well-known for the central Coronet cluster near the R CrA star (Loren 1979; Taylor & Storey 1984; Wilking et al. 1986; Brown 1987). Large-scale C¹⁸O 1–0 maps show that it contains about 50 M_\odot of gas and dust (Harju et al. 1993). Many surveys have been undertaken in the IR (e.g., Wilking et al. 1986; Wilking et al. 1997; Olofsson et al. 1999; Nisini et al. 2005), but only a few studies mapped this region at submillimeter wavelengths (Chini et al. 2003; Nutter et al. 2005). Although Corona Australis has only a few protostars with rising infrared SEDs, the cloud does contain some of the most luminous low-mass protostars in the neighborhood of the Sun ($D < 200$ pc) with luminosities of up to 20 L_\odot .

In this paper we present observations of submillimeter lines of CO and HCO⁺ of a sample of 16 embedded sources in the southern sky, with a focus on the Chamaeleon I and Corona Australis clouds, to identify basic parameters such as column density, presence and influence of outflowing material, presence of warm and dense gas and the influence of the immediate surroundings, in preparation for *Herschel* and ALMA surveys or in-depth high resolution interferometric observations. In Sect. 2 we present the observations, for which the results are given in Sect. 3 with a distinction between the clouds and isolated sources. Both the single spectra (Sect. 3.1) and maps (Sect. 3.2) are presented. In Sect. 4 we perform the analysis of the observations, making use of archival submillimeter continuum data, with the final conclusions given in Sect. 5.

¹ This publication is based on data acquired with the Atacama Pathfinder Experiment (APEX) with programs E-77.C-0217, E-77.C-4010 and E-78.C-0576. APEX is a collaboration between the Max-Planck-Institut für Radioastronomie, the European Southern Observatory, and the Onsala Space Observatory.

Table 1. Source sample.

Source	RA (h m s) [J2000]	Dec (d m s) [J2000]	Dist. (pc)	Lum. (L_{bol})	Ref. ^a	Notes ^c
Chamaeleon I						
Ced 110 IRS 4	11 06 47.0	-77 22 32.4	150 ^e	1	1,2,3	ISO-Cha 84
Ced 110 IRS 6	11 07 09.6	-77 23 04.3	150	0.6	1,3	ISO-Cha 92
Cha IRS 6a	11 07 09.9	-77 23 06.3	150	0.8	4	ISO-Cha 92+
Cha IRN	11 08 37.1	-77 43 51.0	150	5	3	ISO-Cha 150
Cha INa 2	11 09 36.6	-76 33 39.0	150	0.6	5	
Corona australis						
RCrA IRS 5	19 01 48.0	-36 57 21.6	170 ^e	2	6,14	SMM 5
HH 100 ^b	19 01 50.7	-36 58 10	170	15	6,14	SMM 3
RCrA IRS 7A	19 01 55.2	-36 57 21.0	170	3.3 ^d	7,14	SMA 2, SMM 1C
RCrA IRS 7B	19 01 56.2	-36 57 27.0	170	17 ^d	7,14	SMA 1, SMM 1B
RCrA TS 3.5	19 02 07.1	-36 53 26.2	170	–		
CrA IRAS 32	19 02 58.7	-37 07 34.5	170	3.4	14	ISO-CrA 182, SMM 8
Isolated						
HH 46	08 25 43.8	-51 00 35.6	450 ^f	16	8,9,10	BHR 36
IRAS 07178-4429	07 19 21.8	-44 34 55.1	–	–	10,11	CG1/BHR 17
IRAS 12496-7650	12 53 17.2	-77 07 10.6	200 ^g	50	12	DK Cha, Cham II
IRAS 13546-3941	13 57 42.2	-39 56 21.0	550 ^h	–	10,11	CG12/BHR 92
IRAS 15398-3359	15 43 01.3	-34 09 15.0	130 ⁱ	0.92	2,13	B228, Lupus

^a References: 1. Luhman et al. (2008); 2. Froebrich (2005); 3. Persi et al. (2000); 4. Persi et al. (2001); 5. Persi et al. (1999); 6. Nisini et al. (2005); 7. Groppi et al. (2007); 8. Noriega-Crespo et al. (2004); 9. Velusamy et al. (2007); 10. Bourke et al. (1995); 11. Santos et al. (1998); 12. van Kempen et al. (2006); 13. Evans et al. (2005); 14. Nutter et al. (2005); ^b observations of HH 100 were erroneously pointed at coordinates: RA 19h01m49.1s, Dec -36d58m16.0s. See text for further discussion; ^c other names and cloud location; ^d the luminosities of the two RCrA IRS 7 sources are not well determined, due to confusion of the total integrated flux at far-IR wavelengths. The total luminosity of both sources ($20 L_{\odot}$) was used in the characterisation; ^e Knude & Høg (1998); ^f Heathcote et al. (1996); ^g Hughes & Hartigan (1992); ^h Maheswar et al. (2004); ⁱ Murphy et al. (1986).

2. Technical information

2.1. Source list

Sources were selected from a sample of sources with rising infrared SEDs (Class I) observed with the InfraRed Spectrograph (IRS) on *Spitzer* in the scope of the c2d legacy program (Evans et al. 2003) and with the very large telescope (VLT) of the European Southern Observatory (Pontoppidan et al. 2003) (Table 1). At the time of selection of the *Spitzer* and VLT sources in 2000, the list included the bulk of the known southern low-mass Class I YSOs with mid-infrared fluxes of at least 100 mJy. Most of these sources are located in the Chamaeleon and Corona Australis clouds, supplemented by a few other isolated Class I sources found initially by IRAS. Within the Chamaeleon I cloud, most sources are located in the Cederblad region (Persi et al. 2000; Hiramatsu et al. 2007). Cha IRS 6a is located 6'' away from Ced 110 IRS 6 (~half an APEX beam at 460 GHz). Ced 110 IRS 4 was studied by Belloche et al. (2006) which detect an outflow with an axis of $<30^{\circ}$, which makes this source a prime target in Chamaeleon. The embedded YSOs in the Corona Australis region are mostly located in the small region around R CrA, called the Coronet (Wilking et al. 1986; Wilking et al. 1997; Nutter et al. 2005), but two sources are located in the R CrA B region. RCrA IRS 7A and B are believed to be two embedded objects in a wide binary configuration with a separation of 30'' (Nutter et al. 2005; Schöier et al. 2006). These are deeply embedded as little to no IR counterparts were found (Groppi et al. 2007). HH 100 is in a region that is dominated by the RCrA A complex, but is an embedded source in itself according to Nutter et al. (2005). CrA IRAS 32 is located in R CrA B region, but has little to none known surrounding material. HH 46 is a Class I protostar famous for its well-characterized outflow,

pointed to the south-west (Chernin & Masson 1991; Heathcote et al. 1996; Stanke et al. 1999; Noriega-Crespo et al. 2004; Velusamy et al. 2007). It is extensively discussed in van Kempen et al. (2009a). IRAS 12496-7650, also known as DK Cha, is one of the brightest protostars in the southern hemisphere and a potential driving source of HH 54 (van Kempen et al. 2006). ISO-LWS observations were detected with ISO (Giannini et al. 1999), but not confirmed by van Kempen et al. (2006). IRAS 07178-4429, IRAS 13546-3941 and IRAS 15398-3359, all very interesting embedded sources in the southern hemisphere, are also included (e.g., Bourke et al. 1995; Shirley et al. 2000; Haikala et al. 2006). Table 1 lists the sources of our sample and their properties. Luminosities are adopted from the c2d lists (Evans et al. 2003, 2009) and the VLT lists (Pontoppidan et al. 2003).

During the reduction, it was discovered that the original position of HH 100 was incorrect and differed by $\sim 20''$ from the IR position. Throughout this paper, the incorrect position will be referred to as “HH 100-off”, while “HH 100” will refer to the actual source. Single-pixel spectra for HH 100-off are shown in some of the figures, as they are useful as probes of the cloud material and outflows in the RCrA region, whereas the true HH 100 source position is included in the maps.

2.2. Observations

Observations of the sources in Table 1 were carried using the APEX-2a (345 GHz, Risacher et al. 2006) and the First Light APEX Submillimeter Heterodyne (460/800 GHz, denoted as FLASH hereafter, Heyminck et al. 2006) instruments mounted on APEX between August 2005 and July 2006. FLASH allows for the simultaneous observation of molecular lines in the 460 GHz and 800 GHz atmospheric windows.

Table 2. Overview of the APEX observations.

Line	Instrument	Cloud ^a	Note
¹² CO	3–2	APEX-2a	Cha, CrA, Iso.
	map	APEX-2a	80'' × 80''
	4–3	FLASH-I	
	map	FLASH-I	40'' × 40''
	7–6	FLASH-II	
map	FLASH-II	40'' × 40''	
C ¹⁸ O	3–2	APEX-2a	Cha, CrA, Iso.
HCO ⁺	4–3	APEX-2a	Cha, CrA, Iso.
H ¹³ CO ⁺	map	APEX-2a	80'' × 80''
	4–3	APEX-2a	
	4–3	APEX-2a	Cha, CrA, Iso.

^a Cha = Chamaeleon, CrA = Corona Australis and Iso. = Isolated sample.

Using APEX-2a, observations were taken of the ¹²CO 3–2 (345.796 GHz), C¹⁸O 3–2 (329.331 GHz), HCO⁺ 4–3 (356.734 GHz) and H¹³CO⁺ 4–3 (346.998 GHz) molecular lines of the entire sample at the source position with the exception of Cha IRS 6a in ¹²CO. The ¹²CO 4–3 (461.041 GHz) and 7–6 (806.652 GHz) transitions were observed with FLASH for the Chamaeleon I sample as well as some of the isolated sample (Ced 110 IRS 4, Ced 110 IRS 6, Cha INa 2, Cha IRN, HH46, IRAS 12496-7650 and IRAS 15398-3359). The single spectra of CO 3–2, C¹⁸O 3–2, CO 4–3 and 7–6 for IRAS 12496-7650 can be found in van Kempen et al. (2006), but the integrated intensities are included here for completeness. Similarly, HH 46 is discussed more extensively in van Kempen et al. (2009a). Typical beam sizes of APEX are 18'', 14'' and 8'' at 345, 460 and 805 GHz with respective main beam efficiencies of 0.73, 0.6 and 0.43 (Güsten et al. 2006).

For both instruments, new fast Fourier transform spectrometer (FFTS) units were used as back-ends, with over 16 000 channels available (Klein et al. 2006), allowing flexible observations up to a resolution of 60 kHz (0.05 km s⁻¹ at 345 GHz). Pointing was checked using line pointing on nearby point sources and found to be within 3'' for the APEX-2a instrument. The pointing of FLASH was not as accurate with excursions up to 6'' for these observations. However, it is not expected that this has significant influences on the results, as most spectra were extracted from the peak intensities of the maps. Calibration was done on hot and cold loads as well as on the sky. Total calibration errors are of the order of 20%. Reference positions of 1800'' to 5000'' in azimuth were selected. For RCrA IRS 7 and 5, emission in the CO 3–2 line at this position was subsequently found resulting in artificial absorption in the spectra, but this did not exceed 5% of the source emission and is less than the calibration uncertainty.

Observations at APEX were taken under normal to good weather conditions with the precipitable water vapor ranging from 0.4 to 1.0 mm. Typical system temperatures and integration times were 600 and 1000 K and 5 and 4 min for APEX-2a and FLASH-I, respectively. All spectra at a given position were summed and a linear baseline was subtracted within the CLASS package. The APEX-2a observations were smoothed to a spectral resolution of 0.2 km s⁻¹. The rms was found to be 0.15–0.2 K in 0.2 km s⁻¹ channels for HCO⁺ 4–3, ¹²CO 3–2 and C¹⁸O 3–2. H¹³CO⁺ spectra were re-binned to 0.5 km s⁻¹ for deriving the (upper limits on) integrated intensity. The rms for the CO 4–3 observations is 0.35 K and for CO 7–6 1.4 K in channels of 0.3 km s⁻¹, significantly higher than the APEX-2a observations because of the higher system temperatures.

In addition to single spectra, small (up to 80'' × 80'') fully sampled maps were taken using the APEX-2a instrument (see Table 2) of ¹²CO 3–2 and HCO⁺ 4–3 for HH 46, Ced 110 IRS 4, CrA IRAS 32, RCrA IRS 7 and HH 100. With FLASH, similar maps were taken of the Cha I sample, HH 46 and IRAS 12496-7650 in ¹²CO 4–3 and 7–6, but not of the RCrA sample. All maps were taken in on the fly (OTF) mode and subsequently rebinned to 6''. The rms in the maps is a factor of 5 or more higher than that in the single spectra. For example, for the CO 4–3 maps taken with FLASH the noise levels are ~0.9 K in a 0.7 km s⁻¹ channel, compared with 0.35 K in a 0.3 km s⁻¹ for the single position spectra.

For IRAS 15398-3359, maps were also taken with the 16-pixel heterodyne array receiver HARP-B mounted on the James Clerk Maxwell telescope (JCMT)² in the CO 3–2, C¹⁸O 3–2 and HCO⁺ 4–3 lines. The high spectral resolution mode of 0.05 km s⁻¹ available with the ACSIS back-end was used to disentangle foreground material from outflowing material. Spectra were subsequently binned to 0.15 km s⁻¹. The HARP-B pixels have typical single side-band system temperatures of 300–350 K. The 16 receivers are arranged in a 4 × 4 pattern, separated by 30''. This gives a total footprint of 2' with a spatial resolution of 15'', the beam of the JCMT at 345 GHz. The 2' × 2' fields were mapped using the specifically designed jingle mode HARP4³. Calibration uncertainty is estimated at about 20% and is dominated by absolute flux uncertainties. Pointing was checked every two hours and was generally found to be within 2–3''. The map was re-sampled with a pixel size of 5'', which is significantly larger than the pointing error. The main-beam efficiency was taken to be 0.67. The JCMT data for IRAS 15398-3359 are presented in Sect. 3.3.

All APEX data were reduced using the CLASS reduction package⁴. For the JCMT data the STARLINK package GAIA and the CLASS package were used.

3. Results

3.1. APEX single spectra at source position

Spectra are shown in Figs. 1–4 (all spectra taken with APEX-2a), and Fig. 5 (spectra taken with FLASH). The integrated intensities and peak temperatures at the source positions are given in Tables 3 (CO and C¹⁸O observations with APEX-2a and FLASH observations) and 4 (HCO⁺ and H¹³CO⁺ with APEX-2a). Source velocities are determined with an accuracy of 0.1 km s⁻¹ by fitting Gaussian profiles to the optically thin lines of H¹³CO⁺ (preferred if detected) or C¹⁸O. The results are presented in Table 4. Table 3 also includes the width of the C¹⁸O 3–2 line, if detected. These are generally narrow, of order 1 km s⁻¹.

In general the 3–2 and 4–3 lines of ¹²CO cannot be fitted with single Gaussians, because of self-absorption at or around the source velocity V_{LSR} . This absorption is especially deep in RCrA IRS 7A and 7B with $\tau \ll 1$. Due to this absorption, the total integrated line strength of ¹²CO spectra is not useful in the analysis of the quiescent molecular gas. Only for a few sources, e.g. IRAS 07178-4429, can the ¹²CO 3–2 be fitted with a single

² The James Clerk Maxwell Telescope is operated by The Joint Astronomy Centre on behalf of the Science and Technology Facilities Council of the United Kingdom, the Netherlands Organisation for Scientific Research, and the National Research Council of Canada. Data were obtained with programs M06BN11, M07BN09 and M08AN05.

³ See JCMT website <http://www.jcmt.jach.hawaii.edu/>

⁴ CLASS is part of the GILDAS reduction package. See <http://www.iram.fr/IRAMFR/GILDAS> for more information.

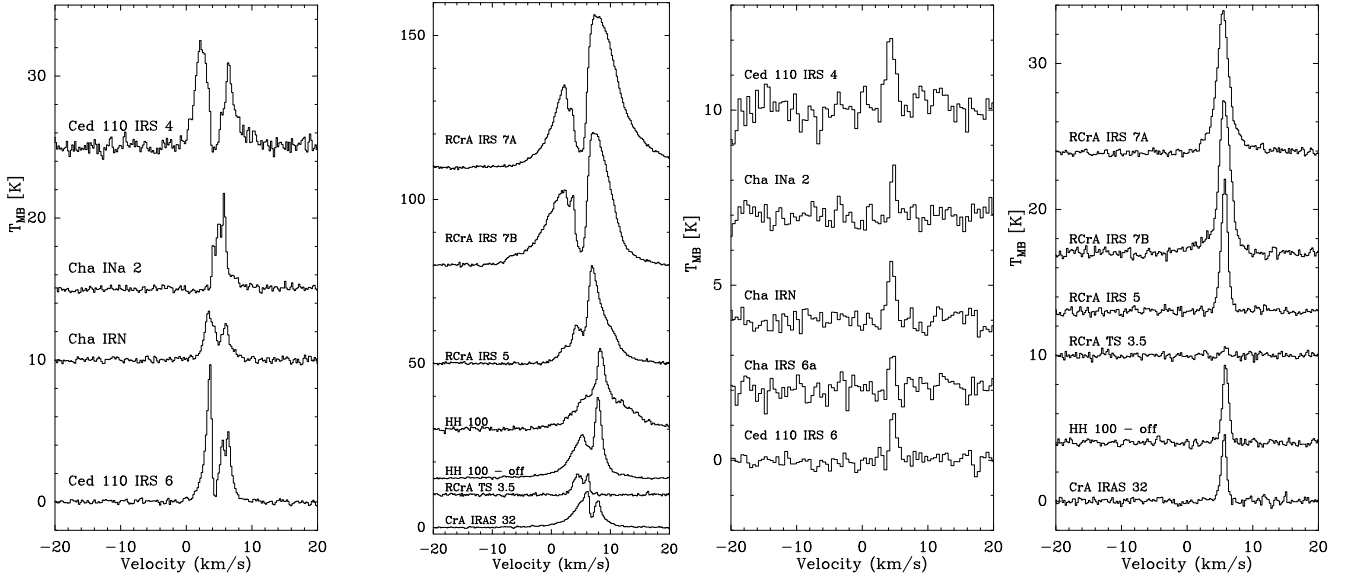


Fig. 1. ^{12}CO 3–2 spectra of the sources in Chamaeleon (*far left*) and Corona Australis (*middle left*) and C^{18}O 3–2 spectra of the sources in Chamaeleon (*middle right*) and Corona Australis (*far right*). Spectra in this and subsequent figures are offset for clarity.

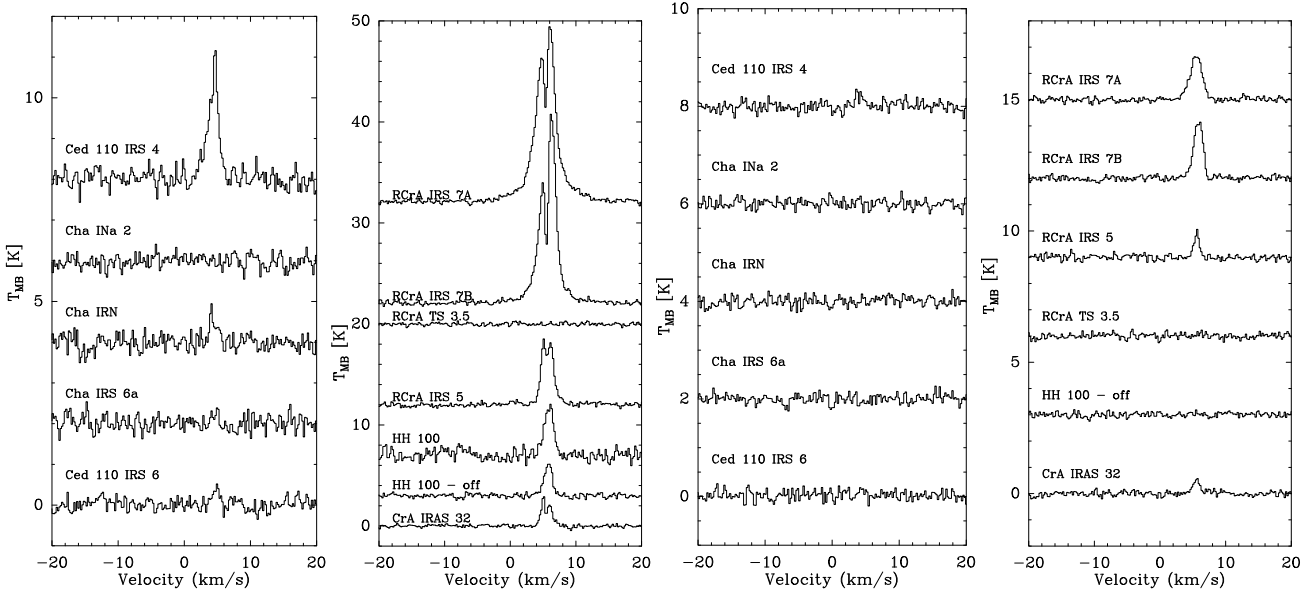


Fig. 2. HCO^+ 4–3 spectra of the sources in Chamaeleon (*far left*) and Corona Australis (*middle left*), as well as H^{13}CO^+ 4–3 spectra of the sources in Chamaeleon (*middle right*) and Corona Australis (*far right*).

Gaussian. Interestingly, the self-absorption is absent in all three detected CO 7–6 lines in Ced 110 IRS 4, Cha INa 2 and Cha IRN at the S/N level of the observations. All C^{18}O 3–2 lines can be yfitted with single Gaussians, indicating that there are no unrelated (foreground) clouds along the line of sights. The C^{18}O 3–2 lines are much stronger in the R CrA cloud than in the other clouds.

The majority of the sources show strong line wings, a sign of a bipolar outflow. Especially the sources in RCrA have prominent emission up to 15 km s^{-1} from the line center.

The HCO^+ lines, which can be used to trace the dense gas, cover the widest range of antenna temperatures and include a variety of line profiles. As two extreme cases, no HCO^+ 4–3 is seen toward Cha INa2 down to 0.2 K , whereas the spectrum for RCrA IRS 7A peaks at $T_{\text{MB}} = 18 \text{ K}$. Note that the brightest spectra in Corona Australis all show self-absorption, indicating

that the HCO^+ 4–3 is optically thick at the positions of the envelope. Ced 110 IRS 4, RCrA IRS 7A and 7B and CrA IRAS 32 have line profiles suggesting dense outflowing gas. The H^{13}CO^+ 4–3 line is only detected for 5 sources, although the detection of Ced 110 IRS 4 is only 3.4σ .

3.2. APEX maps

The maps of the total integrated intensities of HCO^+ 4–3 can be found in Figs. 6 and 7, alongside outflow maps of ^{12}CO 3–2. In the outflow maps, the integrated spectrum is split between red-shifted (*dashed contour*), quiescent (*not shown*) and blue-shifted (*solid contour*). The three components are separated by $\pm 1.5 \text{ km s}^{-1}$ from the systemic velocity (see Table 4). Different methods for separating the outflow and quiescent components were tested but these did not change the results within the

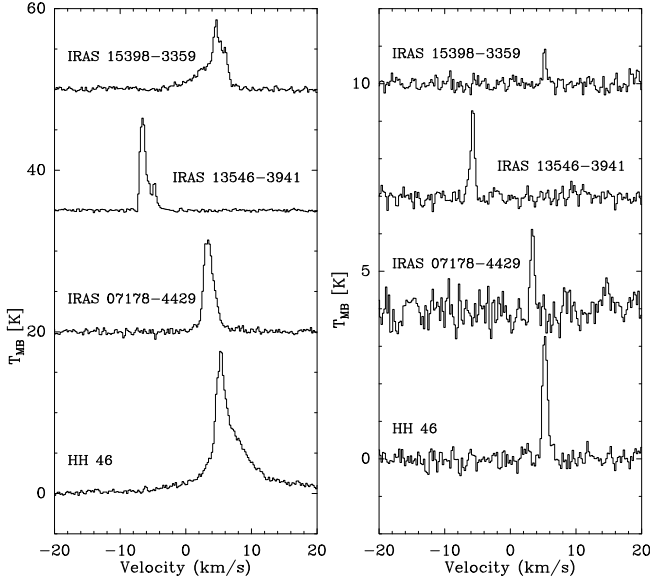


Fig. 3. $^{12}\text{CO } J = 3-2$ (left) and $\text{C}^{18}\text{O } 3-2$ (right) spectra for the isolated sample.

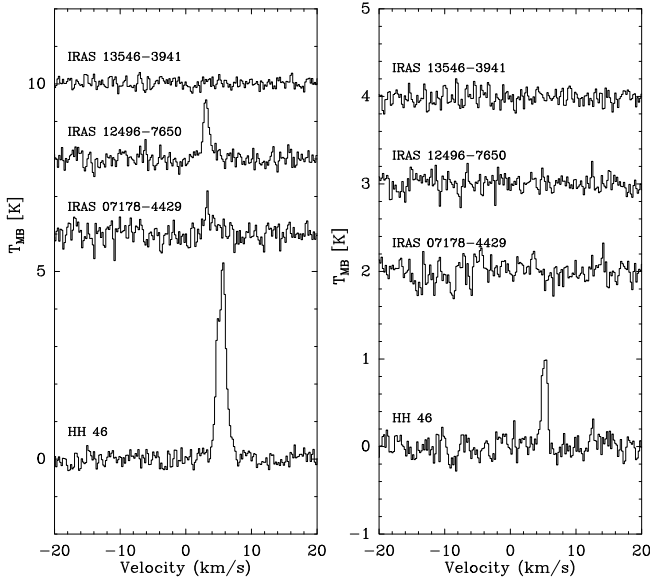


Fig. 4. $\text{HCO}^+ J = 4-3$ (left) and $\text{H}^{13}\text{CO}^+ 4-3$ (right) spectra for the isolated sample.

overall uncertainties. The integrated intensity maps of CO 4–3 are shown in Fig. 8. These are comparable to the CO 3–2 maps, but not with the HCO^+ 4–3 maps.

The HCO^+ 4–3 and CO 3–2 maps for Ced 110 IRS 4 and CrA IRAS 32 (see Fig. 6) show spatially resolved cores, centered on the known IR position. For both sources, outflow emission is seen originating at the source position. HH 100 (Fig. 6) shows no HCO^+ 4–3 core, but does have outflowing gas in the CO 3–2 map, originating at the IR position (marked with a X). There is strong HCO^+ emission north of HH100, which does not correspond to any source in the Nutter et al. (2005) SCUBA maps. At this moment, this discrepancy cannot be explained. The maps around RCrA IRS 7A and 7B (Fig. 7, sources marked with X and centered on RCrA IRS 7A) show a single elongated core in the HCO^+ map that is up to $60''$ along the major axis. Both sources lie firmly within the core. The $^{12}\text{CO } 3-2$ outflow is centered on RCrA IRS 7A, suggesting it is the driving

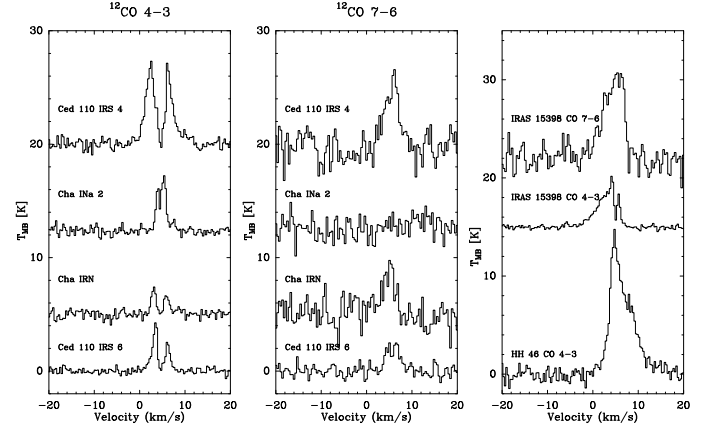


Fig. 5. $^{12}\text{CO } J = 4-3$ (left) and $7-6$ (middle) spectra of the sources in Chamaeleon, as well as the spectra of HH 46 and IRAS 15398-3359 taken with FLASH (right).

source. HH 46 (Fig. 7) shows a nearly circular core in HCO^+ , but a strongly outflow-dominated emission profile in CO 3–2, with much stronger red-shifted than blue-shifted emission. For more information, see van Kempen et al. (2009a). The CO 4–3 integrated intensity maps show elongated spatial profiles for Ced 110 IRS 4, Ced 110 IRS 6 and Cha IRN, but no peak for Cha Ina 2. IRAS 12496-7650 shows a round core, dominated by outflow emission (see Sect. 4.3.3)

3.3. JCMT map of IRAS 15398-3359

Figure 9 shows the spectrally integrated intensity maps of CO 3–2, HCO^+ 4–3 and $\text{C}^{18}\text{O } 3-2$ around the position of IRAS 15398-3359. The maps clearly show a single core around the central position, which is completely spatially resolved. There is little to no C^{18}O or HCO^+ emission outside of the core, while the CO 3–2 has emission lines at around 10 K in the surrounding cloud. The C^{18}O map, which lacks outflow emission, is somewhat shifted to the south from the other two maps. The spectra at the central source position taken from these maps can be found in Fig. 10. The CO spectra are dominated by the blue-shifted outflow. The integrated intensity of HCO^+ 4–3 can be found in Table 4. The independently calibrated CO 3–2 spectra taken with JCMT HARP-B differ from the spectrum taken with APEX-2a by only 3% in integrated intensity, well within the stated calibration uncertainties of both telescopes.

4. Analysis

4.1. Envelope properties

Assuming the (sub-)mm emission is dominated by the cold dust in the protostellar envelope, its mass can be derived from dust continuum observations (Shirley et al. 2000; Jørgensen et al. 2002). Using the SCUBA Legacy archive (Di Francesco et al. 2008), envelope masses were derived for YSOs in Corona Australis. Henning et al. (1993) observed fluxes at 1.3 mm for a large sample in Chamaeleon using the SEST, which are used here to constrain the masses of the very southern sources. All masses were derived using the relation

$$M_{\text{tot}} = S_{\nu} D^2 / \kappa_{\nu} B_{\nu}(T_{\text{d}}) \quad (1)$$

assuming an isothermal sphere of 20 K, a gas-to-dust ratio of 100 and a dust emissivity κ_{ν} at $850 \mu\text{m}$ of $0.02 \text{ cm}^2 \text{ g}^{-1}$ (gas+dust)

Table 3. ^{12}CO and C^{18}O results^a.

Source	^{12}CO 3–2		C^{18}O 3–2			CO 4–3		CO 7–6	
	$\int T_{\text{MB}} dV^d$ (K km s ⁻¹)	T_{MB} (K)	$\int T_{\text{MB}} dV^d$ (K km s ⁻¹)	T_{MB} (K)	ΔV (km s ⁻¹)	$\int T_{\text{MB}} dV^d$ (K km s ⁻¹)	T_{MB} (K)	$\int T_{\text{MB}} dV^d$ (K km s ⁻¹)	T_{MB} (K)
Chamaeleon									
Ced 110 IRS 4	30.7	7.5	3.7	2.1	1.5	29.8	7.5	24.8	6.9
Ced 110 IRS 6	20.0	9.3	1.6	1.4	1.1	9.7	4.9	8.8	2.5
Cha IRS 6a	–	–	1.2	1.1	1.0	–	–	–	–
Cha IRN	11.1	3.5	2.3	1.8	1.2	6.5	3.0	14.0	5.2
Cha INa 2	11.3	6.7	1.3	1.6	0.8	10.0	4.7	<1.5	–
Corona australis									
CrA IRAS 32	51.6	11.0	4.6 ^e	4.4	1.0	–	–	–	–
HH 100-off	102.6	24.7	6.3	5.2	1.1	–	–	–	–
RCrA IRS 5	144.2	29.9	11.4	8.7	1.2	–	–	–	–
RCrA IRS 7A	406.0	46.4	22.5	8.9	2.2	–	–	–	–
RCrA IRS 7B	332.7	40.4	23.0	10.0	2.2	–	–	–	–
RCrA TS 3.5	16.8	6.4	<0.3	–	–	–	–	–	–
Isolated									
HH 46 ^c	82.5	19.4	3.2	3.3	0.9	70.5	14.9	46.5	8.6
IRAS 07178-4429	24.0	11.4	1.7	2.3	0.7	–	–	–	–
IRAS 12496-7650 ^b	92.8	25	9.2	1.9	1.1	90.0	23	43.7	19.2
IRAS 13546-3941	16.3	11.4	1.8	2.3	0.7	–	–	–	–
IRAS 15398-3359	25.8	9.0	0.5	1.2	0.4	19.9	5.6	45.3	8.5

^a Integrated intensities are across the entire line profile; ^b from van Kempen et al. (2006); ^c CO 7–6 from van Kempen et al. (2009a); ^d calibration uncertainties estimated at 20% dominate the uncertainty of the integrated intensity; ^e this is a significant discrepancy from the value reported in Schöier et al. (2006), which determined this intensity to be 6.5 K km s⁻¹. A possible explanation can be the inaccurate calibration during science verification of Schöier et al. (2006).

Table 4. HCO^+ and H^{13}CO^+ results.

Source	HCO^+ 4–3		H^{13}CO^+ 4–3		V_{LSR}^a (km s ⁻¹)
	$\int T_{\text{MB}} dV^b$ (K km s ⁻¹)	T_{MB} (K)	$\int T_{\text{MB}} dV^b$ (K km s ⁻¹)	T_{MB} (K)	
Chamaeleon					
Ced 110 IRS 4	4.0	3.1	0.38	0.25	4.3
Ced 110 IRS 6	0.5	0.4	<0.06	–	4.8
Cha IRS 6a	<0.2	–	<0.06	–	4.6
Cha IRN	0.87	0.95	<0.06	–	4.5
Cha INa 2	<0.2	–	<0.06	–	4.8
Corona australis					
CrA IRAS 32	4.1	2.9	0.72	0.53	5.6
HH 100-off	4.8	3.2	<0.06	–	5.9
RCrA IRS 5	14.2	7.0	0.96	0.86	5.7
RCrA IRS 7A	63.7	17.4	3.8	1.6	5.5
RCrA IRS 7B	49.0	18.7	3.8	2.2	5.7
RCrA TS 3.5	<0.2	–	<0.06	–	5.9
Isolated					
HH 46	8.4	5.4	1.1	1.0	5.3
IRAS 07178-4429	1.0	0.6	<0.08	–	3.4
IRAS 12496-7650	1.9	1.5	<0.06	–	1.9
IRAS 13546-3941	<0.12	–	<0.06	–	-5.7
IRAS 15398-3359 ^c	5.9	4.6	–	–	5.2

^a The rest velocity V_{LSR} was determined by fitting Gaussians to either the H^{13}CO^+ 4–3 (preferred) or C^{18}O 3–2 lines (see Table 3); ^b calibration uncertainties estimated at 20% dominate the uncertainty of the integrated intensity; ^c data from HARP-B map.

from Ossenkopf & Henning (Col. 5, 1994). To scale to 1.3 mm, the dust emissivity was assumed to scale with frequency as $\kappa_\nu \propto \nu^{1.5}$ following the results from Ossenkopf & Henning (1994). The mass of the HH 46 envelope is estimated at $\sim 5 M_\odot$ using new LABOCA observations and radiative transfer modelling (van Kempen et al. 2009a). For IRAS 12496-7650, LABOCA data of Cha II was used (Nefs et al., in prep.) The radii R_{core} over which S_ν is calculated are taken to be the core radii from Di Francesco et al. (2008). Such radii are not the FWHM of the

cores, but are quite close to the radius where the temperature reaches 10 K (Jørgensen et al. 2002). No mass could be derived for Cha IRS 6a, RCrA TS 3.5, IRAS 07178-4429, Cha INa2 and IRAS 13546-3941 as they were not detected or observed. The estimated envelope masses are given in Table 5. They range from 0.04 to 6.3 M_\odot . For Corona Australis, our masses are a factor of three lower than those by Nutter et al. (2005). Differences are due to the difference in assumed dust temperature of 12 vs 20 K, as well as a different dust emissivity κ_ν at 850 μm .

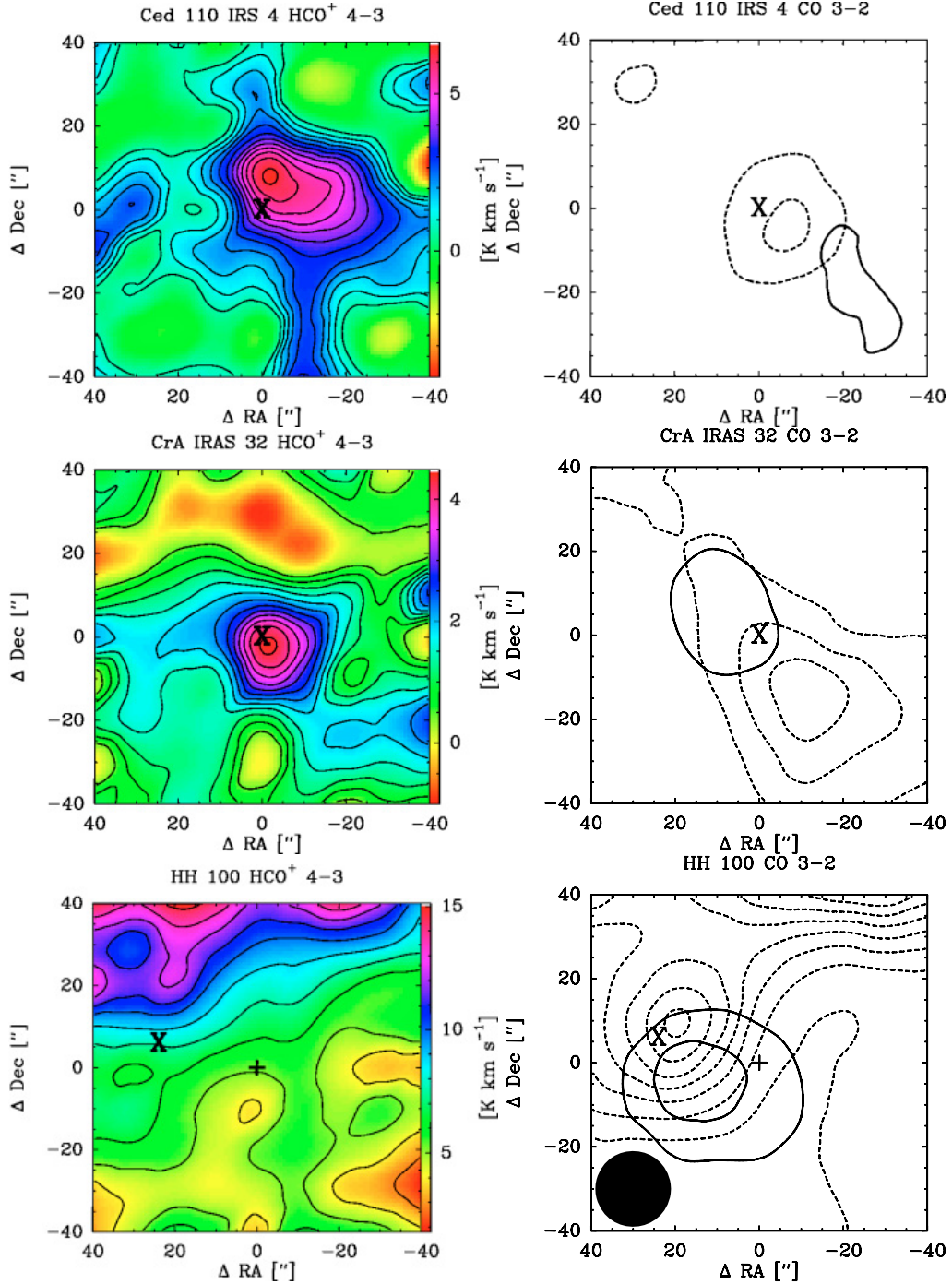


Fig. 6. HCO^+ $J = 4-3$ (left) and $\text{CO } 3-2$ (right) maps of Ced 110 IRS 4 (top), CrA IRAS 32 (middle) and HH 100 (bottom). The maps are $80'' \times 80''$ in size. HCO^+ $4-3$ is integrated over the entire line. $\text{CO } 3-2$ shows the red- (dashed lines) and blue-shifted (solid lines) parts of the emission, derived by integrating the line wings of each spectral line (velocity difference greater than 1.5 km s^{-1} w.r.t. the systemic velocity). Contour levels for the $\text{CO } 3-2$ map are at $3\sigma, 6\sigma, 9\sigma, \dots$ with σ equal to the noise levels of 0.3 K km s^{-1} . The HCO^+ contours are plotted at 10%, 20%, 30%, ... of the maximum intensity given in Table 4. The 10% level corresponds to 7σ for Ced 110 IRS4, 4σ for CrA IRAS 32 and 9σ for HH 100. The APEX beam is shown in the lower right image. The IR position of HH 100 is marked with a “X”, while the pointed position HH100-off is marked with a plus sign.

With the assumption that the H^{13}CO^+ $4-3$ and $\text{C}^{18}\text{O } 3-2$ emission is optically thin, one can estimate the column densities of these molecules in the protostellar envelope. In this calculation, an excitation temperature of 20 K is assumed, based on the average temperature within the protostellar envelope, for both the envelope and cloud material. Table 5 gives the column densities of H_2 , C^{18}O and H^{13}CO^+ , where the H_2 column density is derived from the C^{18}O column density assuming a H_2/CO

ratio of 10^4 and a $^{16}\text{O}/^{18}\text{O}$ ratio of 550 (Wilson & Rood 1994). The H_2 column densities range from a few times 10^{22} cm^{-2} in Chamaeleon to a few times 10^{23} cm^{-2} in Corona Australis, all in a $18''$ beam. However, freeze-out of CO onto the interstellar grains make the adopted ratio of H_2 over CO a lower limit. In very cold regions ($T < 15 \text{ K}$), abundances can be as much as two orders of magnitude lower than the assumed CO/H_2 abundance of 10^{-4} . For sources where continuum data at $850 \mu\text{m}$ are

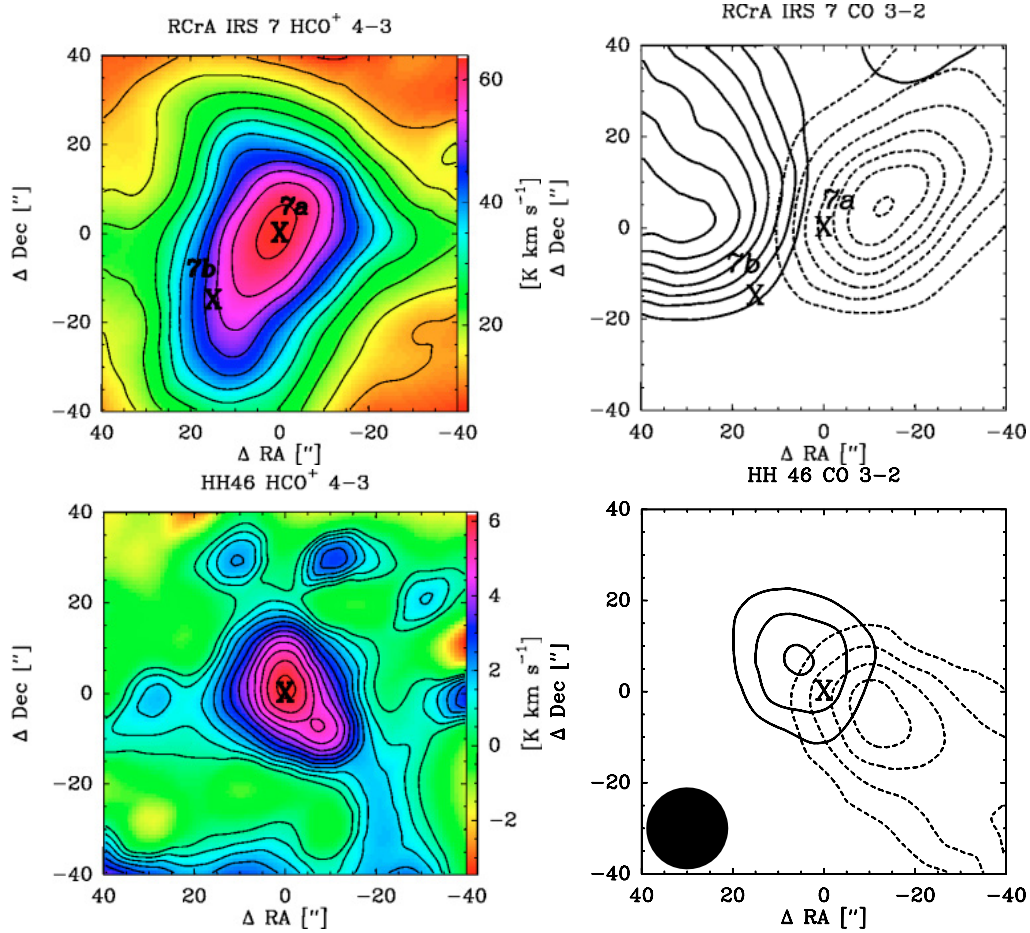


Fig. 7. HCO^+ $J = 4-3$ (left) and $\text{CO } 3-2$ (right) maps of RCrA IRS 7 (top) and HH 46 (bottom). The maps are $80'' \times 80''$ in size. HCO^+ $4-3$ is integrated over the entire line. $\text{CO } 3-2$ shows the red- (dashed lines) and blue-shifted (solid lines) emission, derived by integrating the line wings (velocity difference greater than 1.5 km s^{-1} w.r.t. the systemic velocity) of each spectral line. Contour levels for the $\text{CO } 3-2$ map are at $3\sigma, 6\sigma, 9\sigma, \dots$ with σ equal to 0.3 K km s^{-1} . The HCO^+ contours are plotted at 10%, 20%, 30%, ... of the maximum intensity given in Table 4. The 10% level corresponds to 25σ for RCrA IRS 7, and 5σ for HH 46. The APEX beam is shown in the lower right image. Both RCrA IRS 7A and IRS 7B are shown with X in the CO map, but the map is centered on RCrA IRS 7A.

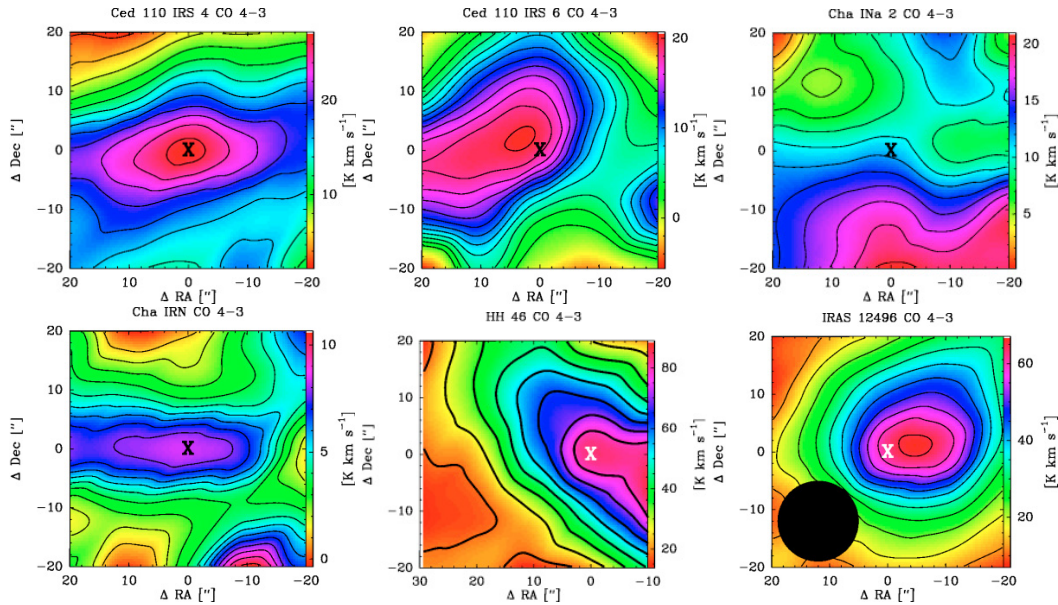


Fig. 8. $\text{CO } J = 4-3$ integrated intensity maps taken with FLASH of Ced 110 IRS 4, Ced 110 IRS 6 and Cha InA2 (top row), and Cha IRN, HH 46 and IRAS 12496-7650 (bottom row). Note that the noise levels in these maps are higher than in the spectra given in Fig. 5. Source positions are marked with “X”. The APEX beam is shown in the lower right image. The lines are drawn to guide the eye.

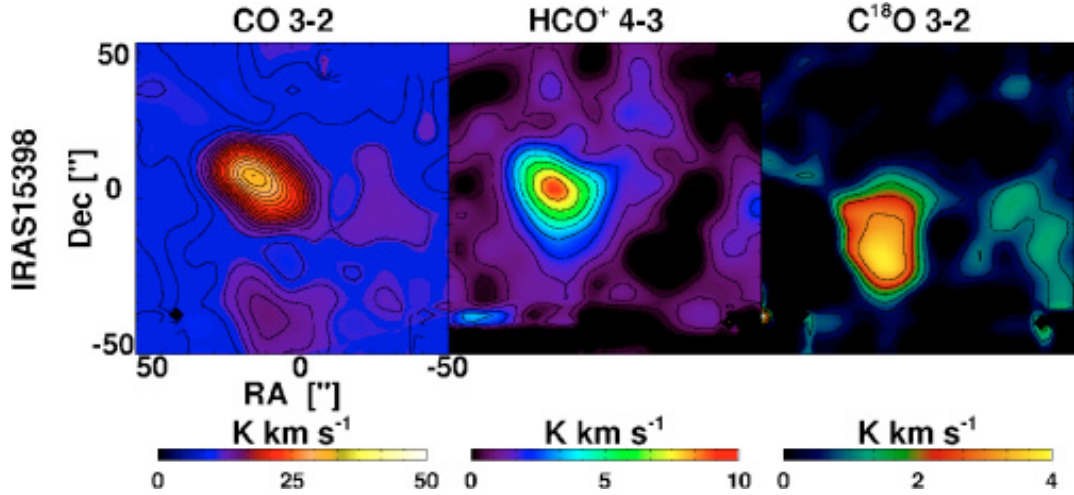


Fig. 9. The spectrally integrated intensities of CO 3–2 *left*, HCO⁺ 4–3 *middle* and C¹⁸O 3–2 *right* observed toward IRAS 15398–3359 with HARP-B on the JCMT. Spectra were integrated between velocities of –5 and 15 km s^{–1}. The source itself is at 5.2 km s^{–1}. The cores are all slightly resolved, compared to the 15'' beam of the JCMT.

Table 5. Overview of the envelope properties^a.

Source	R_{core} ($''$)	M_{envelope} (M_{\odot})	$N(\text{H}_2)^a$ (10^{22} cm^{-2})	$N(\text{C}^{18}\text{O})$ (10^{15} cm^{-2})	$N(\text{H}^{13}\text{CO}^+)$ (10^{15} cm^{-2})	$\tau_{\text{CO}3-2}$	τ_{HCO^+4-3}
Chamaeleon							
Ced 110 IRS 4	20	0.07	5.0/–	8.3	1.4	181	6.7
Ced 110 IRS 6	20	0.04	3.3/–	5.5	–	90	<13
Cha IRS 6a	–	–	0.26/–	0.43	–	–	–
Cha IRN	20	0.17	4.3/–	7.2	–	400	<5.2
Cha INa 2	–	–	3.8/–	6.3	–	150	–
Corona australis ^b							
CrA IRAS 32	44	0.8	10.5/21.2*	17.5	3.0	257	16
HH100-off	45	1.6	12.4/35.2*	20.7	–	130	<0.9
RCrA IRS 5	43	1.7	20.7/24.5*	35.1	4.8	189	10
RCrA IRS 7A	48	6.3 ^c	21.2/30.5*	35.3	8.9	117	7.7
RCrA IRS 7B	48	6.3 ^c	23.8/30.5*	39.7	12.3	156	10
RCrA TS 3.5	–	–	–/–	–	–	–	–
Isolated							
HH 46 ^d	60	5.1	8.1/18.2*	13.5	6.1	103	16
IRAS 07178-4429	–	–	5.5/–	9.2	–	123.9	<8
IRAS 12496-7650	25	0.4	3.0/–	5.0	–	25	<3.1
IRAS 13546-3941	–	–	5.5/–	9.2	–	123	–
IRAS 15398-3359	25	0.5	1.9/–	3.2	–	79	–

The column density of H₂ is derived from that of C¹⁸O assuming H₂/C¹⁸O = 5.5 × 10⁶. If 850 μm data are available in Di Francesco et al. (2008), column densities based on the dust emission are also computed. These numbers are indicated as the second entry with an asterisk. Both column densities are within the same 18'' beam; ^b mass estimates in the RCrA region may be severely overestimated due to presence of extended cloud material; ^c RCrA IRS 7A and 7B cannot be distinguished in the sub-millimeter continuum maps; the value refers to the core containing both sources; ^d for a thorough discussion on the mass of HH 46, see van Kempen et al. (2009a).

available from Di Francesco et al. (2008), the column density was independently calculated from the dust, assuming a dust temperature of 20 K. These numbers are in general a factor of 2 to 3 higher consistent with some freeze-out of CO, but for some sources the column densities derived from the dust approach those obtained from C¹⁸O.

The isotopologue observations of C¹⁸O and H¹³CO⁺ also allow to estimate the average optical depth τ in the CO 3–2 and HCO⁺ 4–3 lines (Table 5) following the formula of

$$I(\text{CO})/I(\text{C}^{18}\text{O}) = (1 - e^{-\tau}) / (1 - e^{-\tau/550}) \quad (2)$$

with the isotopologue ratios for both C¹⁸O and H¹³CO⁺ taken from Wilson & Rood (1994). For I, the peak temperatures from

Tables 3 and 4 were taken to avoid contributions from outflow material. The optical depths range from 25 to a few hundred in the CO 3–2 and from about 0.9 to 16 for the HCO⁺ 4–3. HCO⁺ 4–3 is still quite optically thick, even though it is associated with just the envelope. One error in the estimates from the optical depths, may be that the C¹⁸O 3–2 and H¹³CO⁺ themselves are not optically thin, but have optical depths of a few. In that case, the optical depth of the main isotope would lower as well. However, observations of even rarer isotopologues, such as C¹⁷O or HC¹⁸O⁺ would be needed.

Recent C¹⁸O 3–2 data of the Ophiuchus cloud show that at many locations throughout L 1688, multiple foreground layers are present providing additional reddening of embedded sources

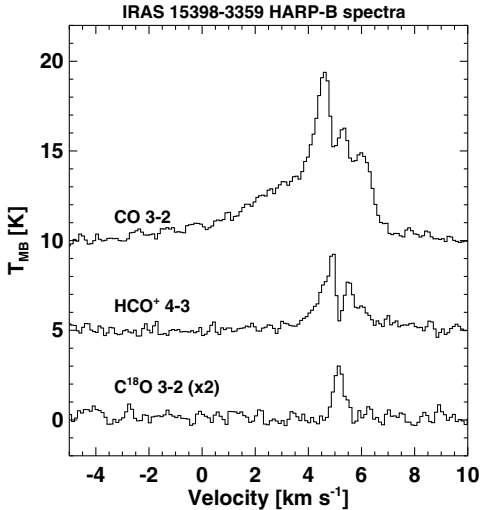


Fig. 10. The spectra of CO 3–2 *top*, HCO+ 4–3 *middle* and C¹⁸O 3–2 *bottom* observed with HARP-B on the JCMT at the central source position.

(van Kempen et al. 2009b). In our sample, all C¹⁸O 3–2 lines can be fitted with single Gaussians indicating that no fore-ground layers are present in any of the observed clouds, in contrast with Ophiuchus.

4.2. Embedded or not?

Analysis of the physical structure of several sources classified as Class I based on their IR spectral slope has shown that some of them are in fact not embedded sources, but rather edge-on disks, such as CRBR 2422.8 (Brandner et al. 2000; Pontoppidan et al. 2005), or IRS 46 (Lahuis et al. 2006). Others turn out to be obscured (background) sources or occasionally even disks in front of a dense core (van Kempen et al. 2009b). Theoretical models from Robitaille et al. (2006) and Crapsi et al. (2008) indeed show that edge-on disks can masquerade as embedded sources in their infrared SED due to the increased reddening.

Following Robitaille et al. (2006) and Crapsi et al. (2008), the border between a truly embedded so-called “Stage 1” source and a “Stage 2” star + disk system is put at accretion rates of $10^{-6} M_{\odot} \text{ yr}^{-1}$, which in the context of these models corresponds to an envelope mass of $\sim 0.1 M_{\odot}$ or a H₂ column of $(2-6) \times 10^{21} \text{ cm}^{-2}$. Because of potential confusion with surrounding (foreground) clouds and disks, one cannot simply use the masses derived from the continuum data but one must look in more detail at the properties of a source. One of the key additional criteria for identification as a truly embedded source is the concentration of warm dense gas around the source. The concentration is determined by the comparison of the peak intensity in a map with the amount of extended emission. Such a parameter has been extensively discussed and successfully applied in the analysis of submillimeter continuum observations from SCUBA (Johnstone et al. 2001; Walawender et al. 2005; Jørgensen et al. 2007). For example, they have shown that pre-stellar cores have much more extended and less concentrated emission than protostellar envelopes.

A recent survey of Class I sources in the Ophiuchus L 1688 region has demonstrated that such a method can be expanded to molecular line mapping and be used as a powerful tool for identifying truly embedded protostars from edge-on disks and

obscured sources (van Kempen et al. 2009b). HCO⁺ 4–3, a high density tracer, proved to be particularly useful. The recipe for proper identification consists of three ingredients. First the peak intensity of HCO⁺ line should be brighter than 0.4 K, a factor of 4 more than is commonly seen for disks (Thi et al. 2004). Second, the concentration parameter of HCO⁺ 4–3 should be higher than 0.6. Third, the HCO⁺ should preferably be extended within the single dish beam. For non-resolved HCO⁺ emission, other information, such as whether or not the source is extended in the submillimeter continuum or whether it has a (compact) outflow, should be taken into account.

The concentration of HCO⁺ is defined as:

$$C_{\text{HCO}^+} = 1 - \frac{1.13 B^2 S_{\text{HCO}^+}}{\pi R_{\text{obs}}^2 T_{\text{int}}}, \quad (3)$$

with S_{HCO^+} the HCO⁺ emission integrated spatially (K km s⁻¹) and spectrally over the entire envelope with radius R_{obs} (in arcseconds), and $T_{\text{int}} = \int T_{\text{MB}} dV$ the HCO⁺ emission integrated spectrally over the central beam B of 18'' alone (in K km s⁻¹). The observed core radius is taken to be the FWHM of the spatial distribution of the integrated HCO⁺ intensity (in arcseconds). These values of R_{obs} , tabulated in Table 6, are often comparable to the core radii found from the continuum data. Although less reliable due to a lower critical density and potential contributions from outflows, the quiescent part of the CO 4–3 emission, which is associated with the central regions of protostellar envelopes, can serve as a diagnostic of the concentration of the warm dense gas in the inner envelope as well. Note that any outflow wings have to be removed.

Table 6 lists the derived concentration parameters for our sources. Of the 12 sources for which such data exist, 6 have concentrations of ~ 0.7 and higher, as well as strong HCO⁺ fluxes above 0.5 K km s^{-1} associated with the sources, characteristic of embedded sources. Three sources (HH 100, IRAS 07178-4429 and IRAS 13546-3941) have no associated HCO⁺ core and thus no concentration. Similarly, Cha INa2 shows no signs of centrally concentrated CO 4–3 emission. Cha IRS 6a, Cha INa2, RCrA TS 3.5, IRAS 07178-4429 and IRAS 13546-3941 all lack HCO⁺ 4–3 emission, even below the limit adopted from Thi et al. (2004), and are thus very likely not embedded YSOs.

HH 100 is an exception. Although no concentration could be calculated for this source as it is not peaking on the HH 100 source position, there is strong extended HCO⁺ emission with at least 7σ , and in some areas up to 50σ . A clear outflow is seen in the CO emission in Fig. 6, thus indicating that HH 100 is an embedded source. This is confirmed from results from Spitzer-IRAC and MIPS (Peterson, priv. comm.). However, the lack of concentration from an envelope is puzzling due to the low optical depth derived for this line at HH100-OFF.

The RCrA IRS 7 binary system was classified as two embedded sources by Groppi et al. (2007). The elongated HCO⁺ spatial emission profile indeed suggests that two envelopes are located close to each other. The concentrations of 0.68 and 0.66 (close to 0.7) together with the strong outflow confirm that both sources are embedded. Similar arguments are used to classify RCrA IRS5 and IRAS 12496-7650 as embedded YSOs. In summary, using our line diagnostics, we have confirmed that eleven of our sixteen Class I sources are truly embedded YSOs, and five sources very likely not.

Table 6. HCO⁺ 4–3 and CO 4–3 core radii and concentrations.

Source	R_{HCO^+} (")	C_{HCO^+}	$R_{\text{CO}(4-3)}$ (")	$C_{\text{CO}(4-3)}$	Emb. ^b
Chamaeleon					
Ced 110 IRS 4	21	0.77	20	0.69	y
Ced 110 IRS 6	–	–	16	0.74	y
Cha IRS 6a	–	–	–	–	n ^d
Cha IRN	–	–	12	0.72	y
Cha INa 2	–	–	–	n.c. ^a	n ^d
Corona australis					
CrA IRAS 32	15	0.78	–	–	y
HH 100	–	n.c. ^a	–	–	y ^c
RCrA IRS 5	–	–	–	–	y ^e
RCrA IRS 7A	25	0.68	–	–	y
RCrA IRS 7B	25	0.66	–	–	y
RCrA TS 3.5	–	–	–	–	n ^d
Isolated					
HH 46	15	0.79	–	–	y
IRAS 07178-4429	–	n.c. ^a	–	–	n
IRAS 12496-7650	–	–	–	–	y ^c
IRAS 13546-3941	–	n.c. ^a	–	–	n
IRAS 15398-3359	22	0.9	–	–	y

^a n.c. = no core associated with source; ^b our assessment whether the source is embedded or not; ^c based on presence of outflow, see Sects. 4.2, 4.3 and Fig. 6; ^d no HCO⁺ detected down to the limit; ^e strong HCO⁺ seen.

4.3. Outflows

4.3.1. Temperatures

If we assume that these line wings fill the beam and are tracing the dominant part of the outflowing gas mass (also known as the swept up gas), then the ratios of emission in the line wings of the CO 3–2, 4–3 and 7–6 profiles at the central position in Table 7 can be compared to model line ratios from Appendix C of van der Tak et al. (2007), derived using statistical equilibrium calculations within an escape probability formalism. The line wings are assumed to be optically thin and filling factors to be the same within the different beams. A quick look at the line wings of CO 3–2 and C¹⁸O 3–2 in the sources in Corona Australis provides an upper limit to the optical depth of the CO line wing of about 3.1 close to the quiescent part of the line. At more extreme velocities, the opacity is probably much lower and indeed optically thin. Optically thin line wings were also shown to be a good assumption for the case of HH 46 by van Kempen et al. (2009a). Kinetic temperatures can then be derived if outflow emission is detected in two of these three lines. Note that an observed ratio leads to a degenerate solution of the kinetic temperature and local density and not a unique solution of the temperature. Thus, some estimate of the local density must be available. Densities in the outer envelope can be estimated from radiative transfer modelling of the dust continuum emission and SED (Ivezić & Elitzur 1997). H₂ densities of a few times 10⁵ cm⁻³ are derived by Jørgensen et al. (2002) for distances of 1500–3000 AU (corresponding to 10–20'' at the distances of Chamaeleon and Corona Australis), but these drop to a few times 10⁴ cm⁻³ at a few thousand AU. These densities are assumed to be comparable to the densities in the swept-up gas at these distances.

At densities above the critical density, $n_{\text{cr}} = 5 \times 10^4$ cm⁻³ for CO 3–2, the gas is thermally excited and a temperature can be inferred directly. For lower densities, the gas is subthermally excited and higher kinetic temperatures are needed to produce similar ratios of the line wings. To estimate the temperatures, two scenarios are presented. In the first, it is assumed that the gas is thermally excited ($n > n_{\text{cr}}$) since densities in the envelope

are near to, or higher than, the CO 3–2 critical density. This is applicable for all sources with the exception of HH 46, for which the central beam extends to about 4500 AU in radius. The kinetic temperatures determined in this way are lower limits. A second scenario is considered by assuming that the densities are of order 10⁴ cm⁻³, closer to typical densities of the surrounding cloud or envelopes at larger radii. In the first scenario, outflow temperatures are on the order of 50 K. An exception is IRAS 15398-3359, which appears to be much warmer (100 K) from both the CO 3–2/4–3 ratio as well as the 4–3/7–6 ratio in the blue outflow. Since we lack CO 4–3 and/or 7–6 data of the red outflow, no temperature could be determined for the red outflow. If densities are lower (scenario 2), derived kinetic temperatures are on the order of 150 K, although for HH 46 (blue) and Ced 110 IRS 6 (both red and blue) the outflow temperatures are consistent with ~80 K. Errors on the outflow temperatures are generally on the order of 25 to 40%, due to the sensitive dependency on density, as well as errors on the estimate of the CO line ratios.

Bow-shock driven shell models by Hatchell et al. (1999) predict temperatures of the swept-up gas by calculating the energy balance between the heating due to the kinetic energy of the expanding momentum-conserving shell and the line cooling of the gas. For parameters typical of the Class 0 L 483 source ($L = 9 L_{\odot}$, $M_{\text{env}} = 4.4 M_{\odot}$), outflow temperatures of 50 to 100 K are found in the inner few thousand AU from the star. Along the bulk of the outflow axis, temperatures are modelled to be 100–150 K. Higher temperatures in excess of a few hundred to a thousand K are predicted only near the bow shocks. The models depend on the local conditions such as dust cooling, density distribution and jet velocity, but most parameters have an influence of the order of a few tens of K on the temperature along most of the outflow. The results in Table 7 agree well with the temperature predictions from Hatchell et al. (1999) and suggest that jet velocities >100 km s⁻¹ are not present, with the exception of IRAS 15398-3359.

Although we assumed the line wings to be optically thin, this is not necessarily the case (e.g., Cabrit & Bertout 1992; Hogerheijde et al. 1998). A more in-depth discussion of the effects of optical depth and density on the kinetic temperatures of

Table 7. Temperature constraints of CO line wings ratios^d.

Source	CO 3–2/4–3		CO 4–3/7–6		T_{outflow} (K) Scenario 1 ^a		T_{outflow} (K) Scenario 2 ^b	
	Red ^c	Blue ^c	Red	Blue	Red	Blue	Red	Blue
Ced 110 IRS 4	1.0	1.2	3.5	–	50	40	170	160
Ced 110 IRS 6	2.2	1.7	–	–	<30	40	50	60
HH46	1.0	1.6–2.0	2.0	–	50	< 40	180	80
IRAS 12496	–	0.8	–	>4	–	50	–	<200
IRAS 15398	–	0.7	–	0.8	–	100	–	>200

^a Lines thermally excited ($n > n_{\text{cr}}$); ^b lines subthermally excited (n assumed to be 10^4 cm^{-3}); ^c red and Blue outflow contributions are calculated by excluding the central 3 km s^{-1} emission; ^d errors on the temperatures are 25%, except for temperatures above 150 K, where it is estimated to be at 40%.

Table 8. Outflow parameters from the CO 3–2 mapping.

Source	i	Mass ^a (M_{\odot})	ΔV_{max}^b (km s^{-1})	R_{out}^b (AU)	$t_{\text{d}}^{b,c}$ (yr)	$\dot{M}^{a,d}$ ($M_{\odot} \text{ yr}^{-1}$)	$F_{\text{CO}}^{a,e}$ ($M_{\odot} \text{ yr}^{-1} \text{ km s}^{-1}$)	$L_{\text{kin}}^{a,f}$ (L_{\odot})
Red lobe								
Ced 110 IRS 4	15	1.4e-2	4.0	2.4e3	2.8e3	4.2e-6	4.6e-5	7e-5
CrA IRAS 32	45	6.6e-2	6.3	9.3e3	7.1e3	9.3e-6	1.3e-4	5.5e-4
HH 100	60	3.6e-1	14.7	> 6.1e3	>2.0e3	<1.5e-4	<4.9e-3	<7.2e-2
RCrA IRS 7	45	1.1e0	23.0	>1e4	>2.1e3	<4.3e-4	<2.2e-2	<5.0e-1
HH46	35	4.3e-1	9.5	>2.5e4	>1.2e4	<3.2e-5	<4.4e-4	<3.1e-3
IRAS 15398-3359	75	2.9e-2	8.2	2.9e3	4.6e3	6.4e-7	6.4e-6	1.6e-5
Blue lobe								
Ced 110 IRS 4	15	5.8e-3	–4.2	–	–	–	–	–
CrA IRAS 32	45	1.7e-2	–5.4	4.6e3	4.0e3	4.3e-6	5e-5	1.8e-4
HH 100	60	4.7e-2	–9.7	4.6e3	2.2e3	2.1e-5	4.4e-4	2.9e-4
RCrA IRS 7	45	1.2e0	–15.8	>5e3	>1.5e3	<7.9e-4	<2.7e-2	<2.9e-1
HH46	35	1.4e-1	–7.4	1.4e4	9.0e3	1.5e-5	1.7e-4	9.3e-4
IRAS 15398-3359	75	9.2e-2	0.7	3.9e3	4.1e4	2.2e-6	3.3e-5	1.2e-4

^a Corrected for inclination using the average correction factors of Cabrit & Bertout (1990); ^b not corrected for inclination; ^c dynamical time scale: $t_{\text{d}} = R/V_{\text{max}}$; ^d mass outflow rate: $\dot{M} = M/t_{\text{d}}$; ^e outflow force: $F_{\text{CO}} = M\dot{V}_{\text{max}}/R$; ^f kinetic luminosity: $L_{\text{kin}} = 0.5 M\dot{V}_{\text{max}}^3/R$.

the swept-up gas in the molecular outflow of HH 46 IRS is presented in van Kempen et al. (2009a). A lower line ratio for the same temperature can also be caused by a higher optical depth in one of the line wings. Similarly a higher density will lead to lower inferred temperatures for the same observed line ratio. Hatchell et al. (1999) also show that there may be a temperature gradient away from the connecting line between bow shock and origin at the protostar. However, this gradient is often diluted out and may be observable within a single beam. The different temperatures of two different ratios may be responsible for this.

4.3.2. Other outflow parameters

For the six sources where outflow emission has been mapped in ^{12}CO 3–2, it is possible to determine the spatial outflow parameters, such as outflow mass, maximum velocity and extent. Subsequently the dynamical time scales and average mass outflow rate, the outflow force (or momentum flux) and kinetic luminosity can be derived following a recipe detailed in Hogerheijde et al. (1998) with the assumption that the emission at the more extreme velocities is optically thin and that the material has kinetic temperatures of 50–80 K. For IRAS 15398-3359 a temperature of 100 K is adopted. The inclination of the outflow with the plane of the sky influences the results and the derived values need to be corrected for their inclination using an average of the model predictions in Cabrit & Bertout (1990). For

HH 46 the inclination has been constrained to 35° (Reipurth & Heathcote 1991; Micono et al. 1998). For the other sources, an inclination is estimated from the distance between the major and minor axes of the maximum contour levels in Figs. 6 and 7 (see Table 8).

The results in Table 8 show that most outflows have masses of 0.01 – $0.1 M_{\odot}$, with average mass loss rates between 2×10^{-6} to $4.4 \times 10^{-4} M_{\odot} \text{ yr}^{-1}$, and outflow forces F_{CO} of 6.4×10^{-6} to $2.7 \times 10^{-2} M_{\odot} \text{ yr}^{-1} \text{ km s}^{-1}$. The strongest outflow is RCrA IRS 7, which produces the highest outflow force and the most kinetic luminosity. This is mainly caused by the fact that emission is detected out to ΔV_{max} as high as 23 km s^{-1} , compared with 4 to 9 km s^{-1} for the other sources, almost an order of magnitude difference. Note that for HH 100 (red only), HH 46 (red only) and RCrA IRS 7 (red and blue), the quoted outflow radius is a lower limit, due to insufficient coverage. The resulting outflow force and kinetic luminosity are thus upper limits. For HH 100 and RCrA IRS 7 subtracting Gaussians with widths of 3 km s^{-1} changes the integrated intensity by 20%. All other parameters depend linearly on the mass M that is derived from the integrated intensity.

Hogerheijde et al. (1998) surveyed the outflows of Class I sources in the Taurus cloud. There, most sources produce weaker outflows than found in Table 8, with outflow forces of the order of a few times $10^{-6} M_{\odot} \text{ yr}^{-1} \text{ km s}^{-1}$, with a few sources having values as high a few times $10^{-4} M_{\odot} \text{ yr}^{-1} \text{ km s}^{-1}$. A recent survey of the outflows present in the Perseus cloud shows

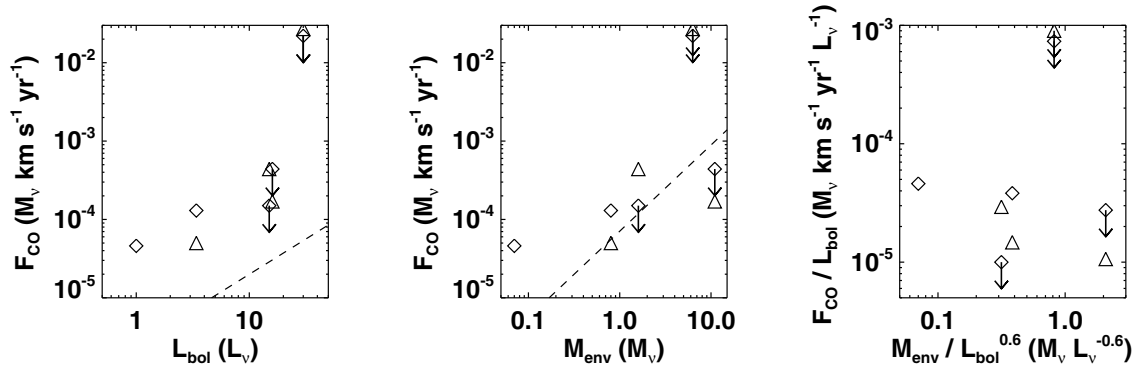


Fig. 11. CO outflow force F_{CO} versus the luminosity, L_{bol} (left), and versus the envelope mass, M_{env} (middle). The right figure shows $F_{\text{CO}}/L_{\text{bol}}$ versus $M_{\text{env}}/L_{\text{bol}}^{0.6}$, which should be free of most luminosity and distance effects following Fig. 7 of Bontemps et al. (1996). Red outflows are shown with diamonds and blue outflows with triangles. The relations between F_{CO} , L_{bol} and M_{env} found by Bontemps et al. are shown with dashed lines.

F_{CO} values of a few times $10^{-7} M_{\odot} \text{ yr}^{-1} \text{ km s}^{-1}$ to a few times $10^{-5} M_{\odot} \text{ yr}^{-1} \text{ km s}^{-1}$ (Hatchell et al. 2007a). However, these numbers were not corrected for inclination, which can account for at least a factor of 5 increase. The observed outflow forces in our sample are all among the upper range of these values, especially HH 100 and RCrA IRS 7. Figure 5 of Hatchell et al. (2007a) shows that most Class I outflows have lower outflow forces than the Class 0 sources.

Most flows observed from the northern hemisphere were first discussed in Bontemps et al. (1996) using CO 2–1 observations with relatively large beams. Outflow forces range from a few times 10^{-7} to $10^{-4} M_{\odot} \text{ yr}^{-1} \text{ km s}^{-1}$, corrected for inclination and optical depth. In Bontemps et al. (1996), a relation between the outflow forces, bolometric luminosities and envelope masses was empirically derived, $\log(F_{\text{CO}}) = -5.6 + 0.9 \log(L_{\text{bol}})$ and $\log(F_{\text{CO}}) = -4.15 + 1.1 \log(M_{\text{env}})$. Figure 11 shows a comparison between the observed outflows of Table 8 and the relations from Bontemps et al. (1996). Although the outflows in our sample are all associated with Class I sources, they are exceptionally strong outflows for their luminosity, but not for their envelope mass. Outflow forces are one to two orders of magnitude higher than expected from the above equation with luminosity. This suggests that the outflow strength as measured through the swept-up material that more about the surroundings (i.e., the amount of matter that can be swept up) than about the intrinsic source and outflow properties.

4.3.3. The outflow of IRAS 12496-7650

An outflow was identified from the line profiles in van Kempen et al. (2006) and it was concluded that the emission as seen with ISO-LWS (Giannini et al. 2001) has to originate on scales larger than $8''$ and not from the inner regions of a protostellar envelope around IRAS 12496-7650. Figure 12 reveals that the detected blue-shifted outflow is located only in the central $15''$ and is peaking strongly on the source. The lack of red-shifted emission reinforces the conclusion that the outflowing gas is viewed almost perfectly face-on and that our line of sight is straight down the outflow cone.

4.3.4. The outflow of IRAS 15398-3359

The line profiles of IRAS 15398-3359 have a clear blue outflow component, with red-shifted emission not seen until further off source. If only the line wings are mapped, Figure 13 shows that

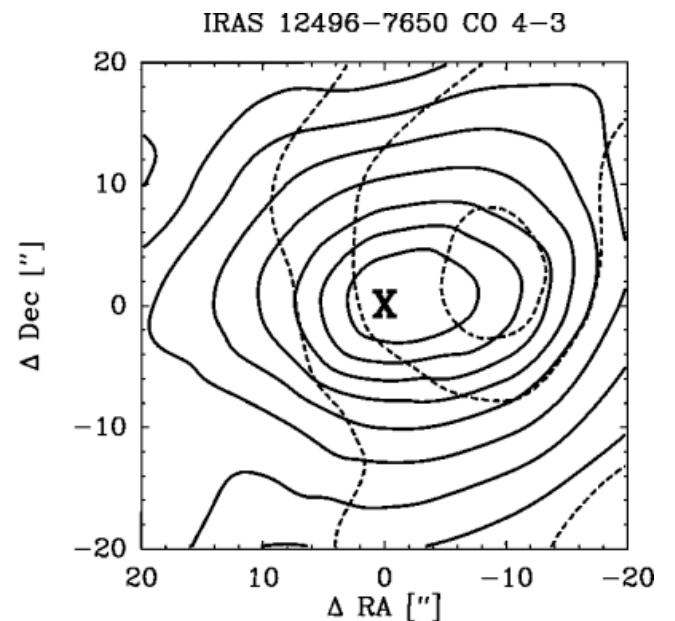


Fig. 12. CO $J = 4-3$ map of IRAS 12496-7650. The blue and red-shifted outflow emission are shown in solid and dashed contours respectively in steps of 10% of the maximum of 34.8 K km s^{-1} .

the outflow of IRAS 15398-3359 is small and extends only $\sim 25''$ across the sky. As discussed above, the blue part of the outflow is exceptionally warm, with significant outflow emission seen in the CO 7–6 line. Although it is smaller in extent, the outflow does not stand out w.r.t to the others in terms of outflow properties as measured from their CO 3–2 maps.

5. Conclusions

We present observations of CO, HCO^+ and their isotopologues, ranging in excitation from CO 3–2 to CO 7–6 of a sample of southern embedded sources to probe the molecular gas content in both the protostellar envelopes and molecular outflows in preparation for future ALMA and Herschel surveys. The main conclusions are the following:

- HCO^+ 4–3 and CO 4–3 integrated intensities and concentrations, combined with information on the presence of outflows, confirm the presence of warm dense quiescent gas associated with 11 of our 16 sources.

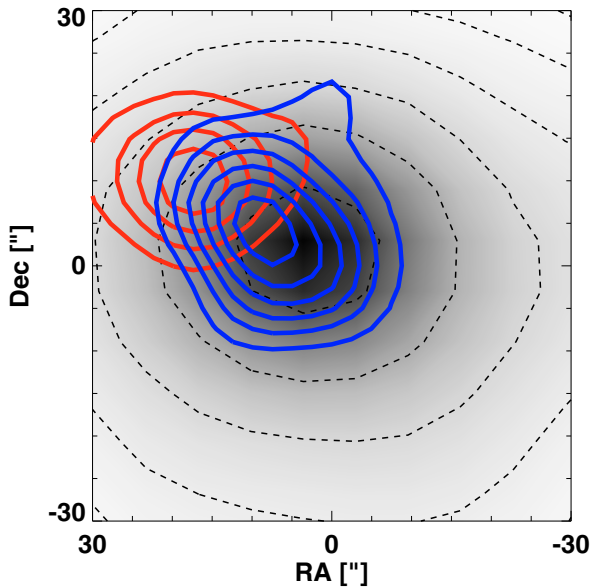


Fig. 13. CO $J = 3-2$ map of IRAS 15398-3359. The blue and red-shifted outflow emission are shown in *blue* and *red* contours respectively in steps of 10% of the maximum of 8.1 K km s^{-1} . The grey-scale and dashed contour lines in the background are the $850 \mu\text{m}$ continuum.

- RCrA TS 3.5, Cha IRS 6a, Cha INa2, IRAS 07178-4429 and IRAS 13546-3941 are likely not embedded YSOs due to the lack of $\text{HCO}^+ 4-3$ emission and/or the lack of central concentration in $\text{HCO}^+ 4-3$.
- The swept-up outflow gas has temperatures of the order of 50–100 K, as measured from the ratios of the CO line profile wings, with the values depending on the adopted ambient densities. These values are comparable to the temperatures predicted by the heating model of Hatchell et al. (1999), with the exception of IRAS 15398-3359, which may be unusually warm.
- The outflows of 6 of our truly embedded sources – Ced 110 IRS 4, CrA IRAS 32, RCrA IRS 7A, HH 100, HH 46, IRAS 15398-3359 – were characterized using CO spectral maps. The outflows all have exceptionally strong outflow forces, almost two orders of magnitude higher than expected from their luminosities following the relation of Bontemps et al. (1996).
- Neither Chamaeleon nor Corona Australis have foreground layers as found in Ophiuchus L 1688. All $\text{C}^{18}\text{O } 3-2$ spectra can be fitted with single Gaussians.

Future observations using ALMA and Herschel will be able to probe the molecular emission associated with these YSOs at higher spatial resolution and higher frequencies. Comparison with single dish data, both continuum surveys and spectral line mapping, will be essential in analyzing the results obtained with future facilities.

Acknowledgements. TvK and astrochemistry at Leiden Observatory are supported by a Spinoza prize and by NWO grant 614.041.004. The APEX staff, in particular Michael Dumke, are thanked for their extensive support and carrying out the observations. We are also grateful for the constructive comments of the anonymous referee.

References

- André, P., Ward-Thompson, D., & Barsony, M. 1993, *ApJ*, 406, 122
- Bachiller, R., & Tafalla, M. 1999, in *The Origin of Stars and Planetary Systems*, ed. C. J. Lada, & N. D. Kylafis (Dordrecht: Kluwer), 227
- Belloche, A., Parise, B., van der Tak, F. F. S., et al. 2006, *A&A*, 454, L51
- Blake, G. A., van Dishoek, E. F., Jansen, D. J., Groesbeck, T. D., & Mundy, L. G. 1994, *ApJ*, 428, 680
- Bontemps, S., André, P., Terebey, S., et al. 1996, *A&A*, 311, 858
- Boogert, A. C. A., Hogerheijde, M. R., Ceccarelli, C., et al. 2002, *ApJ*, 570, 708
- Bourke, T. L., Hyland, A. R., & Robinson, G. 1995, *MNRAS*, 276, 1052
- Brandner, W., Sheppard, S., Zinnecker, H., et al. 2000, *A&A*, 364, L13
- Brown, A. 1987, *ApJ*, 322, L31
- Cabrit, S., & Bertout, C. 1990, *ApJ*, 348, 530
- Cabrit, S., & Bertout, C. 1992, *A&A*, 261, 274
- Chernin, L. M., & Masson, C. R. 1991, *ApJ*, 382, L93
- Chini, R., Kämpgen, K., Reipurth, B., et al. 2003, *A&A*, 409, 235
- Crapsi, A., van Dishoek, E. F., Hogerheijde, M. R., Pontoppidan, K. M., & Dullemond, C. P. 2008, *A&A*, 486, 245
- Damjanov, I., Jayawardhana, R., Scholz, A., et al. 2007, *ApJ*, 670, 1337
- Di Francesco, J., Johnstone, D., Kirk, H., MacKenzie, T., & Ledwosinska, E. 2008, *ApJS*, 175, 277
- Evans, N. J., Allen, L. E., Blake, G. A., et al. 2003, *PASP*, 115, 965
- Evans, II, N. J., Lee, J.-E., Rawlings, J. M. C., et al. 2005, *ApJ*, 626, 919
- Evans, II, N. J., Dunham, M. M., Jørgensen, J. K., et al. 2009, *ApJ*, in press
- Froeblich, D. 2005, *ApJS*, 156, 169
- Giannini, T., Lorenzetti, D., Tommasi, E., et al. 1999, *A&A*, 346, 617
- Giannini, T., Nisini, B., & Lorenzetti, D. 2001, *ApJ*, 555, 40
- Groppi, C. E., Hunter, T. R., Blundell, R., et al. 2007, *ApJ*, 670, 489
- Güsten, R., Nyman, L. Å., Schilke, P., et al. 2006, *A&A*, 454, L13
- Gutermuth, R. A., Myers, P. C., Megeath, S. T., et al. 2008, *ApJ*, 674, 336
- Haikala, L. K., Juvela, M., Harju, J., et al. 2006, *A&A*, 454, L71
- Harju, J., Haikala, L. K., Mattila, K., et al. 1993, *A&A*, 278, 569
- Hartmann, L., Megeath, S. T., Allen, L., et al. 2005, *ApJ*, 629, 881
- Hatchell, J., Fuller, G. A., & Ladd, E. F. 1999, *A&A*, 344, 687
- Hatchell, J., Fuller, G. A., & Richer, J. S. 2007a, *A&A*, 472, 187
- Hatchell, J., Fuller, G. A., Richer, J. S., Harries, T. J., & Ladd, E. F. 2007b, *A&A*, 468, 1009
- Heathcote, S., Morse, J. A., Hartigan, P., et al. 1996, *AJ*, 112, 1141
- Henning, T., Pfau, W., Zinnecker, H., et al. 1993, *A&A*, 276, 129
- Heyminck, S., Kasemann, C., Güsten, R., de Lange, G., & Graf, U. U. 2006, *A&A*, 454, L21
- Hiramatsu, M., Hayakawa, T., Tatematsu, K., et al. 2007, *ApJ*, 664, 964
- Hogerheijde, M. R., van Dishoek, E. F., Blake, G. A., et al. 1997, *ApJ*, 489, 293
- Hogerheijde, M. R., van Dishoek, E. F., Blake, G. A., et al. 1998, *ApJ*, 502, 315
- Hughes, J., & Hartigan, P. 1992, *AJ*, 104, 680
- Ivezić, Z., & Elitzur, M. 1997, *MNRAS*, 287, 799
- Johnstone, D., Wilson, C. D., Moriarty-Schieven, G., et al. 2000, *ApJ*, 545, 327
- Johnstone, D., Fich, M., Mitchell, G. F., et al. 2001, *ApJ*, 559, 307
- Jørgensen, J. K., Schöier, F. L., & van Dishoek, E. F. 2002, *A&A*, 389, 908
- Jørgensen, J. K., Lahuis, F., Schöier, F. L., et al. 2005a, *ApJ*, 631, L77
- Jørgensen, J. K., Schöier, F. L., & van Dishoek, E. F. 2005b, *A&A*, 437, 501
- Jørgensen, J. K., Bourke, T. L., Myers, P. C., et al. 2007, *ApJ*, 659, 479
- Klein, B., Philipp, S. D., Krämer, I., et al. 2006, *A&A*, 454, L29
- Knude, J., & Høg, E. 1998, *A&A*, 338, 897
- Lada, C. J. 1987, in *Star Forming Regions*, ed. M. Peimbert, J. Jugaku, & P. W. J. L. Brand (Reidel, Dordrecht), 115, 1
- Lahuis, F., van Dishoek, E. F., Boogert, A. C. A., et al. 2006, *ApJ*, 636, L145
- Lehtinen, K., Haikala, L. K., Mattila, K., et al. 2001, *A&A*, 367, 311
- Laurini, S., Schilke, P., Menten, K. M., et al. 2004, *A&A*, 422, 573
- Loren, R. B. 1979, *ApJ*, 227, 832
- Luhman, K. L., & Rieke, G. H. 1999, *ApJ*, 525, 440
- Luhman, K. L., Allen, L. E., Allen, P. R., et al. 2008, *ApJ*, 675, 1375
- Maheswar, G., Manoj, P., & Bhatt, H. C. 2004, *MNRAS*, 355, 1272
- Mangum, J. G., & Wootten, A. 1993, *ApJS*, 89, 123
- Maret, S., Ceccarelli, C., Caux, E., et al. 2004, *A&A*, 416, 577
- Micono, M., Davis, C. J., Ray, T. P., Eisloffel, J., & Shetrone, M. D. 1998, *ApJ*, 494, L227
- Motte, F., André, P., & Neri, R. 1998, *A&A*, 336, 150
- Murphy, D. C., Cohen, R., & May, J. 1986, *A&A*, 167, 234
- Nisini, B., Antonucci, S., Giannini, T., et al. 2005, *A&A*, 429, 543
- Noriega-Crespo, A., Morris, P., Marleau, F. R., et al. 2004, *ApJS*, 154, 352
- Nutter, D. J., Ward-Thompson, D., & André, P. 2005, *MNRAS*, 357, 975
- Nutter, D., Kirk, J. M., Stamatellos, D., et al. 2008, *MNRAS*, 384, 755
- Olofsson, G., Hultgren, M., Kaas, A. A., et al. 1999, *A&A*, 350, 883
- Ossenkopf, V., & Henning, T. 1994, *A&A*, 291, 943
- Parise, B., Belloche, A., Leurini, S., et al. 2006, *A&A*, 454, L79
- Persi, P., Marenzi, A. R., Kaas, A. A., et al. 1999, *AJ*, 117, 439

- Persi, P., Marenzi, A. R., Olofsson, G., et al. 2000, *A&A*, 357, 219
- Persi, P., Marenzi, A. R., Gómez, M., et al. 2001, *A&A*, 376, 907
- Pontoppidan, K. M., Fraser, H. J., Dartois, E., et al. 2003, *A&A*, 408, 981
- Pontoppidan, K. M., Dullemond, C. P., van Dishoeck, E. F., et al. 2005, *ApJ*, 622, 463
- Reipurth, B., & Heathcote, S. 1991, *A&A*, 246, 511
- Risacher, C., Vassilev, V., Monje, R., et al. 2006, *A&A*, 454, L17
- Robitaille, T. P., Whitney, B. A., Indebetouw, R., Wood, K., & Denzmore, P. 2006, *ApJS*, 167, 256
- Santos, N. C., Yun, J. L., Santos, C. A., et al. 1998, *AJ*, 116, 1376
- Schöier, F. L., Jørgensen, J. K., van Dishoeck, E. F., et al. 2002, *A&A*, 390, 1001
- Schöier, F. L., Jørgensen, J. K., Pontoppidan, K. M., & et al. 2006, *A&A*, 454, L67
- Shirley, Y. L., Evans, N. J., Rawlings, J. M. C., et al. 2000, *ApJS*, 131, 249
- Shirley, Y. L., Evans, II, N. J., & Rawlings, J. M. C. 2002, *ApJ*, 575, 337
- Snell, R. L., Dickman, R. L., & Huang, Y.-L. 1990, *ApJ*, 352, 139
- Stanke, T., McCaughrean, M. J., & Zinnecker, H. 1999, *A&A*, 350, L43
- Stanke, T., Smith, M. D., Gredel, R., et al. 2006, *A&A*, 447, 609
- Taylor, K. N. R., & Storey, J. W. V. 1984, *MNRAS*, 209, 5P
- Thi, W.-F., van Zadelhoff, G.-J., & van Dishoeck, E. F. 2004, *A&A*, 425, 955
- van der Tak, F. F. S., van Dishoeck, E. F., Evans, N. J., et al. 2000, *ApJ*, 537, 283
- van der Tak, F. F. S., Black, J. H., Schöier, F. L., Jansen, D. J., & van Dishoeck, E. F. 2007, *A&A*, 468, 627
- van Dishoeck, E. F., Blake, G. A., Jansen, D. J., et al. 1995, *ApJ*, 447, 760
- van Kempen, T. A., Hogerheijde, M. R., van Dishoeck, E. F., et al. 2006, *A&A*, 454, L75
- van Kempen, T. A., van Dishoeck, E. F., Güsten, R., et al. 2009a, *A&A*, 501, 633
- van Kempen, T. A., van Dishoeck, E. F., Salter, D. M., et al. 2009b, *A&A*, 498, 167
- Velusamy, T., Langer, W. D., & Marsh, K. A. 2007, *ApJ*, 668, L159
- Walawender, J., Bally, J., Kirk, H., et al. 2005, *AJ*, 130, 1795
- Wilking, B. A., Taylor, K. N. R., & Storey, J. W. V. 1986, *AJ*, 92, 103
- Wilking, B. A., McCaughrean, M. J., Burton, M. G., et al. 1997, *AJ*, 114, 2029
- Wilson, T. L., & Rood, R. 1994, *ARA&A*, 32, 191
- Young, C. H., Shirley, Y. L., Evans, II, N. J., et al. 2003, *ApJS*, 145, 111